Journal of Electron Microscopy **48(6)**: 827–836 (1999)

Full-length paper

Improvement of resolution by maximum entropy linear image restoration for $NiSi_2$/Si interface

Fu-Rong Chen[1,*], J. J. Kai[1], L. Chang[2], J. Y. Wang[3] and W. J. Chen[4]

[1]Center of Electron Microscopy, Dept of Engineering and System Science, National Tsing Hua University, HsinChu, [2]Dept of Materials Science and Engineering, National Chiao-Tung University, HsinChu, [3]Materials R & D Center, CSIST, PO Box 90008-8-5, Lungtan, Taoyuan, and [4]Dept of Mechanical Materials Engineering, National Yun-Lin Polytechnic Institute, Huwei, Yun-Lin, Taiwan

*To whom correspondence should be addressed. E-mail: frchen@msc.nthu.edu.tw

Abstract A linear imaging constrained-maximum entropy method has been developed to extend the resolution from a series of defocused high-resolution images and one diffraction pattern. Our method is basically the Gerchberg–Saxton algorithm, which restores spatial information by imposing real space and Fourier space constraints cyclically. A constrained-maximum entropy method (constrained-MEM) was developed for real space constraints. This constrained-MEM finds an optimum solution of phases such that simulated images resemble the experimental image under some constraints in real space. These constraints include conservation of charge as well as a minimum of the χ^2 function, which is a measure of the level of satisfaction between simulated images and experimental images. For the Fourier space constraint, the square root intensities of diffraction spots were substituted. In this paper, we demonstrate that this method is able to extend the resolution from a series of high-resolution images and one diffraction pattern from a periodic $NiSi_2$/Si interface. The atomic structure of the $NiSi_2$/Si interface can be directly read out from the MEM image without a priori knowledge of the interface.

Keywords maximum entropy, linear image restoration, interfacial structure

Received 30 November 1998, 23 August 1999

Introduction

Interfaces control the properties and the performance of materials, especially the interfaces in sub-half micron devices [1]. Understanding of the interfacial structure on an atomic scale is very important in controlling the processes and properties of thin films in deep sub-micron devices. In the past, high-resolution transmission electron microscopy (HRTEM) has been extensively applied to investigate the atomic structure of such interfaces, for example, as reported by Chen *et al.* [2,3], Hoche *et al.* [4] and Hofmann *et al.* [5]. However, it is well known that the high-resolution image may have no direct relation with the actual atomic structure due to dynamical scattering of the electrons and the spherical aberration and under-focus of the objective lens [6,7]. Furthermore, high frequency information may be truncated by the temporal/spatial coherence of the electron source [6,7]. Finally, the phase in the image plane is lost when the image is recorded. In the past, Coene *et al.* [8], Van Dyck *et al.* [9], Kirkland [10] and Thust *et al.* [11,12] have used a non-linear image reconstruction method to extract the exit wave at the specimen level to recover the structural information to a higher resolution. The exit wave was reconstructed from focal series HRTEM images in their method.

'Direct method' coupling of the HRTEM image and the diffraction intensities has been applied by Ishizuka *et al.* [13], Fan *et al.* [14,15], Hu *et al.* [16], Huang *et al.* [17] and Dong *et al.* [18] to extend the structural information beyond the Scherzer resolution of the TEM. This method is used in X-ray crystallography to extend the structural information based on a set of X-ray diffraction intensities. In these previous works [13–17], the electron intensities were obtained in sufficiently thin specimen regions to avoid dynamical effects and the results were interpreted within the kinematical approximation. Recently, Sinkler

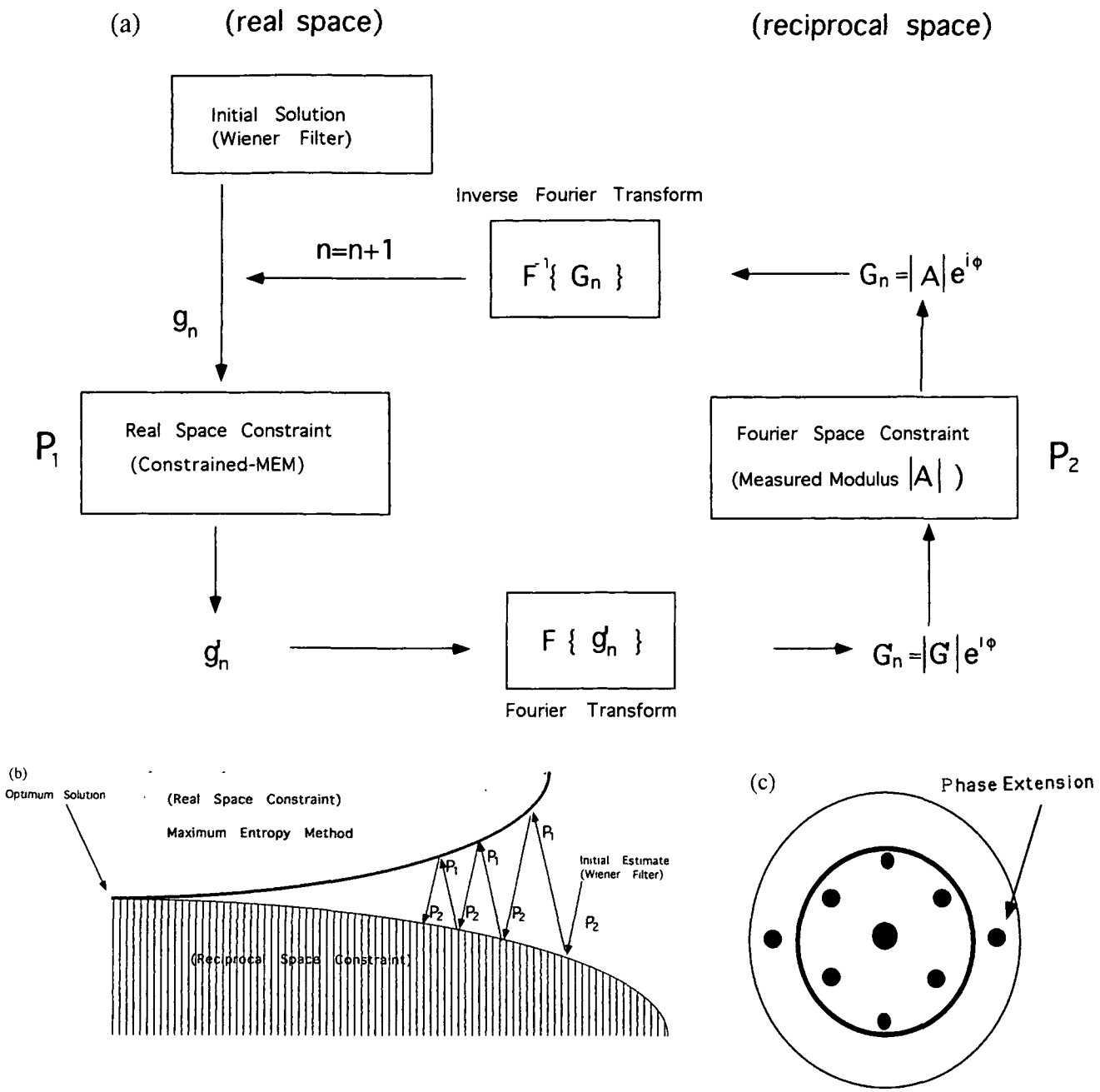

Fig. 1 (a) A flow chart of our algorithm. The real space operation is called P1 projection and the reciprocal space operation is called P2 projection. (See text for detail.) (b) The concept of Gerchberg–Saxton algorithm: cyclic operations of P1 and P2 projections. (c) The phases are actually extended to higher order beams frequency-by-frequency after each P1 projection.

et al. [19] have shown that direct method using dynamical electron diffraction intensities is applicable up to a specimen thickness of 20 nm. As pointed out by these authors [19], direct method using the dynamical intensities does not restore the complex exit wave $\psi(r)$ in real space, but instead the modulus of the Babinet function, or $|1-\psi(r)|$. The Babinet function corresponds to the most probable distribution of atomic peaks, and there is a correlation between the dynamical diffraction intensities and the Fourier components of the Babinet function, a reasonably good approximation to the diffraction wave for moderately thin samples (<20 nm). In the kinematical case, $|1-\psi(r)|$ is proportional to the electrostatic potential $V(r)$ and the Fourier coefficients of $|1-\psi(r)|$ are exactly proportional to the structure factors $|F(h)|$.

Direct method is a set of mathematical techniques, for example, the Sayre equation [20] for determining the phases of the diffracted beams given only amplitude information which is equal to the square root of the measured intensity [21–24]. The maximum entropy algo-

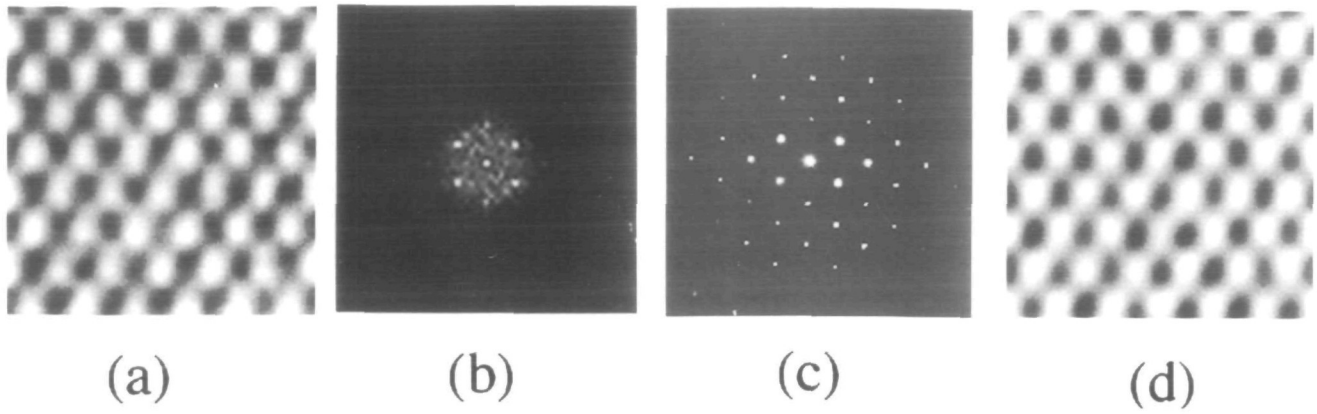

Fig. 2 (a) An experimental HRTEM image of Si alone a <110> zone axis. The defocus value is near Scherzer defocus, –48 nm for a JEOL 4000EX microscope (b) Fourier transform pattern of (a). Only the spots up to {200} can be revealed. (c) An electron diffraction pattern of Si <110> from the region around the HRTEM image. (d) A Wiener filtered image of (a). Its contrast is the reversal of (a).

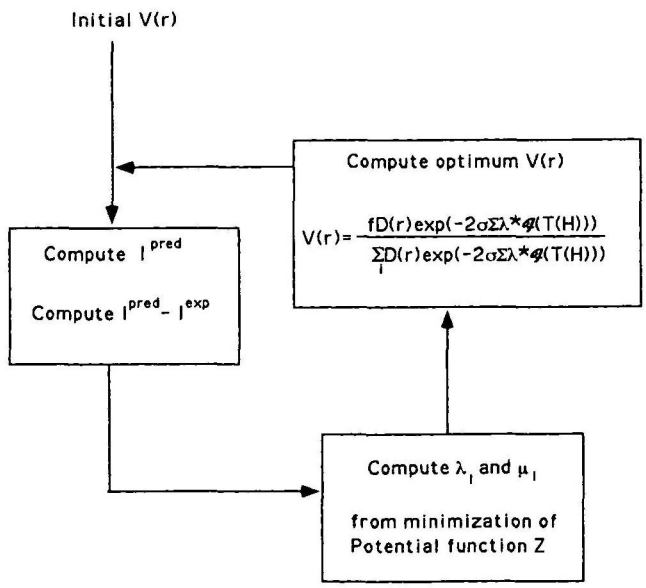

Fig. 3 A flow chart of the constrained-MEM iteration.

Table 1. The amplitude ratios of {002}, {220}, {113}, {222} and {004} *reflections with respect to {111}*

	Measured square root intensity	Theoretical	$\lvert\frac{Fhkl}{F111}\rvert$	Calculated amplitude
{002}	0.1	0		0.01
{220}	0.89	1.09		0.8
{113}	0.56	0.63		0.45
{222}	0.07	0		0.007
{004}	0.51	0.67		0.47

The second column indicates the calculated structural factors and the third column the calculated amplitudes of the diffracted beams for a thickness of 8 nm.

rithm is a direct method technique which has been developed and well discussed by Bricogne [25] for X-ray crystallography. Sinkler *et al.* [19] and Marks *et al.* [26,27] have applied the maximum entropy algorithm using dynamical electron diffraction to solve surface and bulk structures. In previous work by Huang *et al.* [17], a maximum entropy method (MEM) was also used as a de-convolution tool for HRTEM images. In that work, maximum entropy acted as a figure of merit to decide the optimum value of under-focus. In the present paper, we add a linear imaging constraint to the MEM to extend the structural information of HRTEM images of a $NiSi_2$/Si interface.

Our constrained-MEM seeks to improve the phases within input frequencies and to extrapolate optimum phases in higher order diffraction beams such that simulated images of different defocus are close to the experimental images in real space. The optimum phases are proportional to the electrostatic potential V(r) and the Babinet function in the kinematical case. In reciprocal space, the square root intensities of the diffraction spots are substituted into the amplitude part of the Fourier transformation of V(r). The real space and reciprocal space constraints are operated cyclically until the satisfaction level is reached. The level of satisfaction is defined as a χ^2 function, which is a square difference between simulated images and experimental images. The algorithm of this method is basically the Gerchberg–Saxton algorithm [28] which has been developed parallel with but independent of the direct method. In the following section the detail of algorithm and formulation of our method will be described. A HRTEM image of Si [110] will be used as a test of the constrained-MEM algorithm. The application of constrained-MEM to improve the resolution of a series of under-focus high-resolution images of a $NiSi_2$/Si interface will be given. The dumb-bell structure of $NiSi_2$ and Si in projected potential, or the Babinet, can be revealed using constrained-MEM, so that the interfacial structure

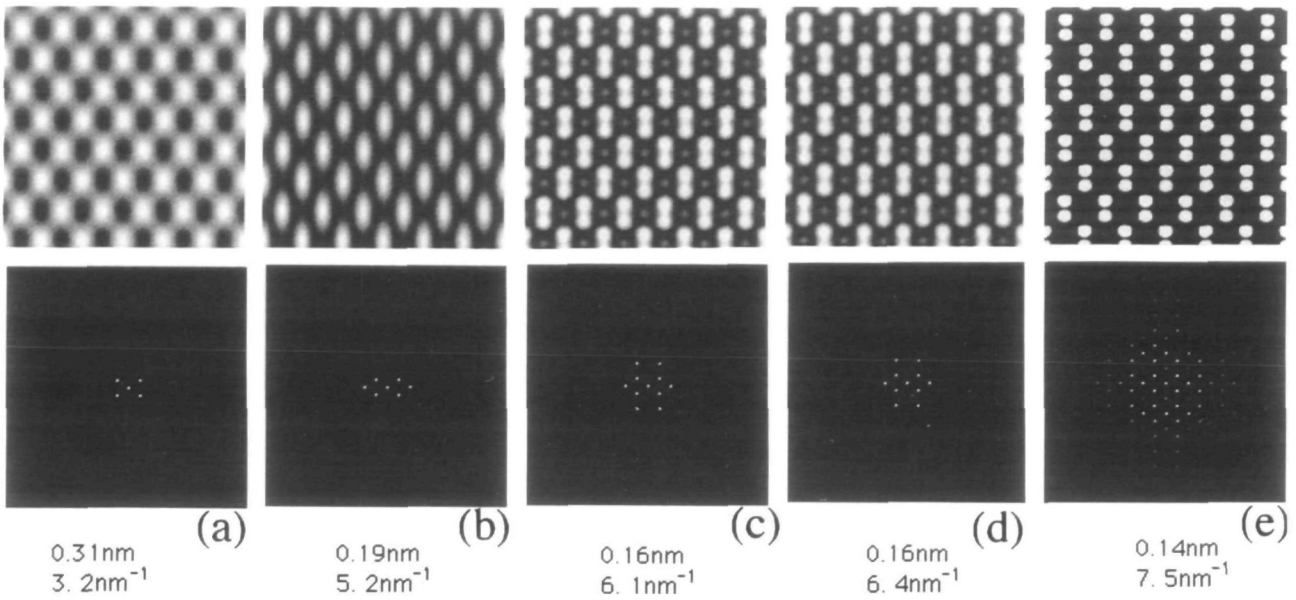

Fig. 4 The resolution of Fig. 2d is extended to different frequencies of (a) 3.2, (b) 5.2, (c) 6.1, (d) 6.4 and (e) 7.6 nm^{-1} using the constrained-MEM. The Fourier transform of each image is also included. The dumb-bell structure is clearly revealed at the frequency of 7.5 nm^{-1}.

of $NiSi_2$/Si can be directly read out without a priori trial interfacial models. The program runs on a Macintosh computer and the source code is written in the script language of Digital Micrograph [29].

Details of the algorithm and formulation

In high-resolution images, high frequency information is attenuated or truncated by the lens contrast transfer function. The phases in the low-order beams are also slightly modified by the lens contrast transfer function. For a regular medium voltage TEM the resolution may be slightly better than 0.2 nm. On the other hand, an electron diffraction pattern usually contains observable diffraction within a limit 0.1 nm, but the information of the phases is lost. Both images and diffraction patterns contain part of the structural information. The task of our method and the other direct methods is to retrieve the information on the phases of the higher order diffraction beams using the HRTEM images and diffraction pattern. The basic procedures of our algorithm are as follows.

(1) A set of starting phases for the low-order beams is obtained from a HRTEM image with the aid of a Wiener filter [30].

(2) The constrained-MEM then finds the optimum phases within the input frequencies and also extrapolates the phases to the next higher frequency. A similar MEM algorithm has been extensively used in the area of astronomy for image deconvolution to improve the resolution of images [31,32].

(3) Fourier transform of the solution from the above step. The square root intensities of the next higher frequency in the diffraction pattern are substituted for the amplitude part of the next higher order beams. The phase part is preserved during this process. An inverse Fourier transformation back to the real space, the Babinet function or the electrostatic projected potential V(r) in the thin specimen case, is extended to the next higher resolution regime.

Procedures (2) and (3) are the real and reciprocal space operations, respectively, and are iterated cyclically until the desired resolution is reached. A flow chart of our procedure is given in Fig. 1a. The g_n serves as input for constrained-MEM in real space. The g'_n is the optimum solution from constrained-MEM in real space. The g'_n have a higher spatial frequency than g_n. This real space operation is called P1 projection. The |G'| and |A| are the amplitudes of the Fourier transform of g'_n and the square root intensities from the diffraction pattern. In reciprocal space, |G'| is substituted by |A| but the ϕ phase part of the Fourier transform of g'_n is saved. This reciprocal space operation is called P2 projection. The spatial resolution is improved by cyclic P1 and P2 operations and is basically the Gerchberg–Saxton algorithm [28] which restores the spatial information by imposing Fourier space and real space constraints cyclically. The concept of the Gerchberg–Saxton algorithm is depicted schematically in Fig. 1b. It is worth mentioning that after P1 projection (constrained-MEM), not only are the phases within the input frequencies improved, but also the phases of the next higher frequency are extrapolated. The phases are actually extended frequency by frequency after each P1 projection. This concept is shown schematically in Fig. 1c.

Procedure (3) is just simply a substitution process. In

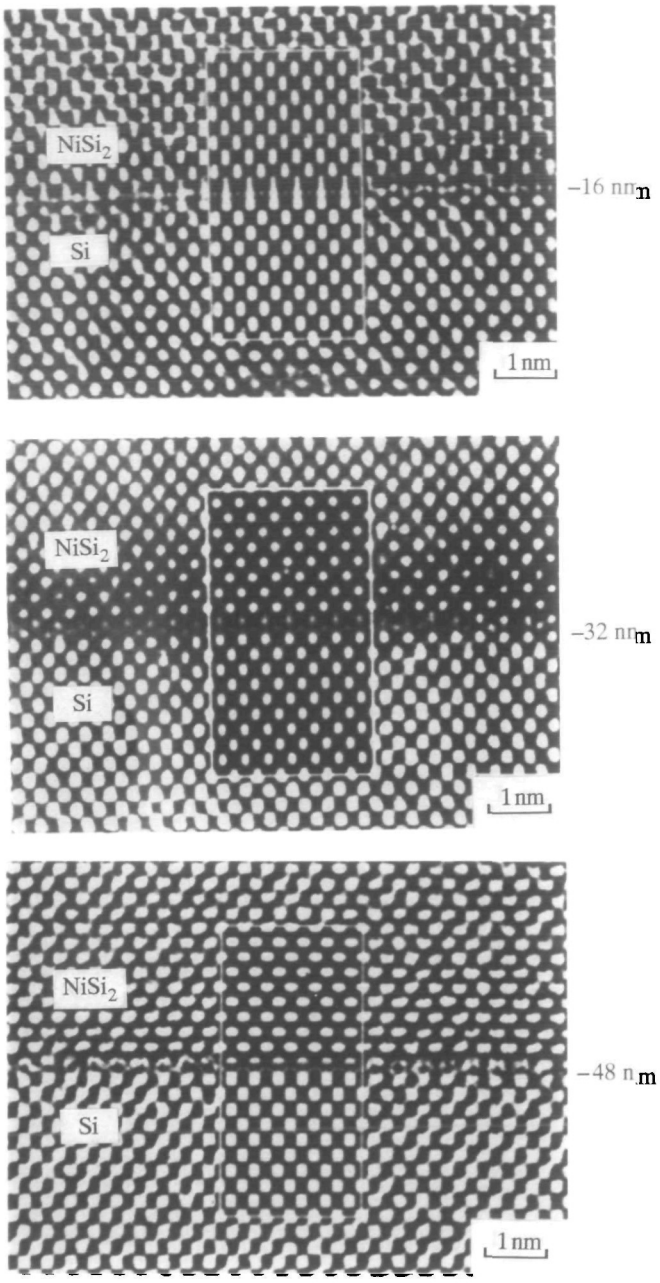

Fig. 5 HRTEM images of $NiSi_2$/Si interfaces recorded under three different under focus values, Δf, (a) −16, (b) −32 and (c) −48 nm, taken near the edge of the specimen along the [110] zone axis.

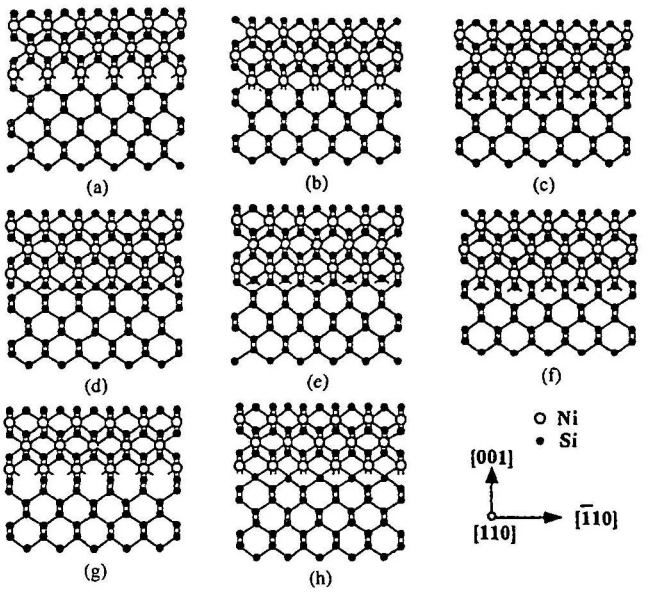

Fig. 6 Eight possible geometrical models of $NiSi_2$/Si deduced from the coincidence-site lattice model.

the following, we will give a detailed description of the theoretical background of procedures (1) and (2).

Wiener filter

Figure 2a shows an experimental HRTEM image of Si along a <110> zone axis. This image was taken using a JEOL 4000EX microscope at the defocus value near Scherzer defocus, −48 nm. This image was taken near the edge of the specimen and the focus value was estimated from the amorphous region at the edge of the specimen. Its Fourier transform pattern is depicted in Fig. 2b. Only the spots up to {200} are revealed. The higher order information is lost from the HRTEM image. The electron diffraction pattern shown in Fig. 2c was also taken from the edge of the specimen, with the selected-area aperture covering a small portion of the specimen and larger portion of empty hole. Both image and diffraction pattern were recorded using imaging plates produced by Fuji Co., Japan [33]. The advantages of the imaging plate are its excellent linearity and dynamic range. When the specimen is thin, the intensity I in the image plane can be approximated as [6]

$$I(r) = 1 + 2\sigma V(r) * F^{-1}(T(H)) \quad (1)$$

where σ is the interaction constant; V(r) is the projected potential, which is related to the projected atomic real space; F^{-1} represents the inverse Fourier transformation; * is the convolution operator; T(H) is the contrast transfer function of the objective lens; and $\underline{H}$ is the reciprocal lattice vector

$$T(H) = \sin(\chi_1(H))\exp(-\chi_2(H)) \quad (2)$$

where

$$\chi_1(H) = \pi\lambda\Delta f H^2 + (1/2)\pi C_s\lambda^3 H^4$$

$$\chi_2(H) = (1/2)\pi^2\lambda^2(\sigma f)^2 H^4 + \pi^2(\alpha^2/\lambda^2)q$$

C_s is the spherical aberration coefficient; λ is the wavelength; δf is focal spread of objective lens; and α is the convergence angle and

$$q = (\lambda\Delta f H + C_s\lambda^3 H^3)^2 \quad (3)$$

For a JEOL 4000EX, C_s = 1.0 mm, focal spread δf = 15 nm and beam divergence α = 0.8 mrad. The Scherzer

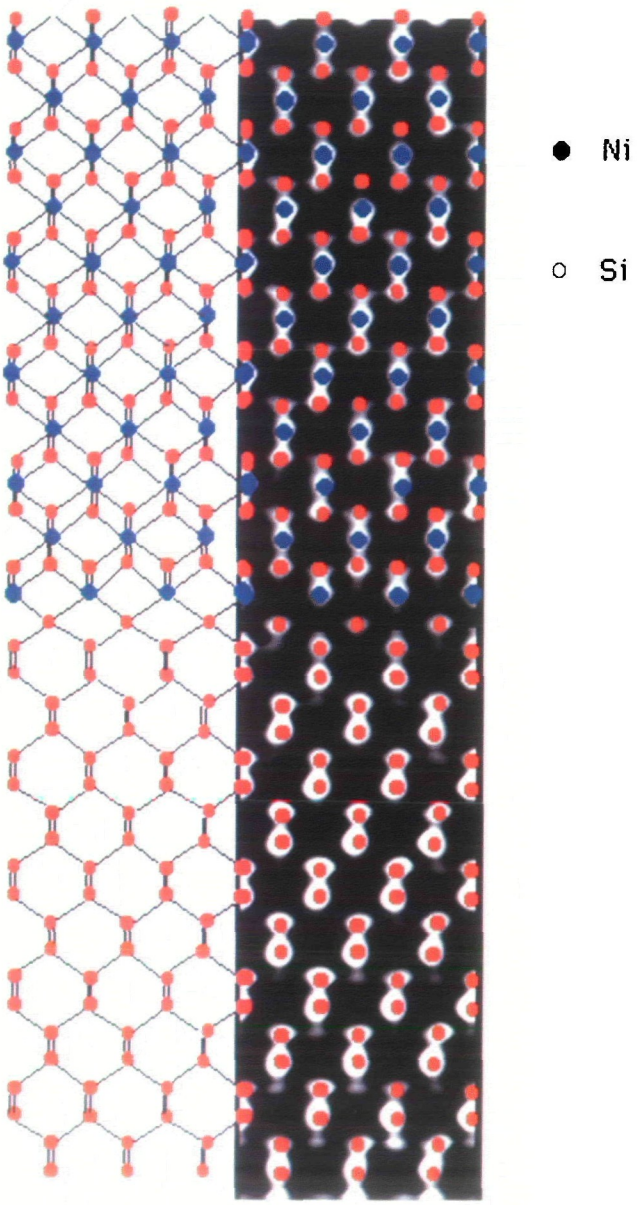

Fig. 7. The MEM deduced V(r) of the $NiSi_2/Si$ interface at a spatial frequency of 7.35 nm^{-1}. Model (h) of Fig. 6 is superimposed with the V(r).

under-focus, $-1.22(C_s\lambda)^{1/2}$ is about –48 nm. Previous works [14] use an inverse filter to obtain the project potential. In this paper, the project potential V(r) is estimated using a Wiener filter [31], given below, to avoid difficulties arising from the zero of T(H):

$$V(r) = \mathbf{F}^{-1}[\mathbf{F}(I(r))(T^*(H)/(T(H)^2 + \kappa)] \quad (4)$$

F is a Fourier transformation operator and T*(H) is the conjugate function of T(H) which is identical to T(H) in this case. κ is related to the noise in the image and can be set to a small constant if the noise is unknown [30]. Figure 2d shows V(r) obtained from (4). The contrast in Fig. 2d is reversed to that in Fig. 2a which confirms that Fig. 2a is a black atom at the Scherzer defocus.

The constrained-MEM algorithm [34]

To deduce the optimum solution of a Babinet function |1–ψ(r)|, or V(r) in the thin specimen case which corresponds to the atomic peaks, we minimize a Lagrangian function $\mathcal{L}$

$$\mathcal{L} = -\sum_i V(r)\ln\left(\frac{V(r)}{D(r)}\right) - \lambda_o\left(\sum_i V(r) - f\right) -$$

$$\sum_j \lambda_j \sum_i [(1 + 2\sigma V(r)*\delta(T(H)) - I_j^e - e_j] - \sum_j \mu_j \left\{\frac{e_j^2}{\sigma_j^2} - \Omega\right\}$$

The first term is defined as the relative entropy S:

$$S = -\sum_i V(r)\ln\left(\frac{V(r)}{D(r)}\right) \quad (5)$$

The relative entropy has proved to be a useful measure of the difference between two probability distributions of V(r) and D(r) [31,32]. D (*x*, *y*) could be an initial potential or a new modified potential Fourier transformed back from the reciprocal space operation. i = 1 . . . n for n pixels of image. j = 1 . . . m for m sets of under-focus conditions.

Three constraints were employed in the MEM algorithm. They are the second, third and fourth terms in the Lagrangian function. The λ_o, λ_j and μ_j are the Lagrangian multipliers for these three constraints.

(1) The charge of the system has to be conserved. The constant f can be determined from summation of intensity from an experimental HRTEM image.

$$\sum_i V(r) = f \quad (6)$$

(2) The optimum solution of V(r) shall make the calculated images at each defocus values as close as possible to the corresponding set of experimental images.

$$\sum_i [(1 + 2\sigma V(r)*\delta(T(H))] = I_j^e - e_j \quad (7)$$

Where I_j^e is the jth experimental image. The e_j is the noise of the jth set image and it usually has a normal distribution [30].

(3) σ_j is the variance of the jth experimental image and Ω is the target χ^2.

$$\sum_j \frac{e_j^2}{\sigma_j^2} = \Omega \quad (8)$$

(4) Setting $\frac{\partial \mathcal{L}}{\partial V(r)} = 0$ and $\frac{\partial \mathcal{L}}{\partial e_j} = 0$, we obtain

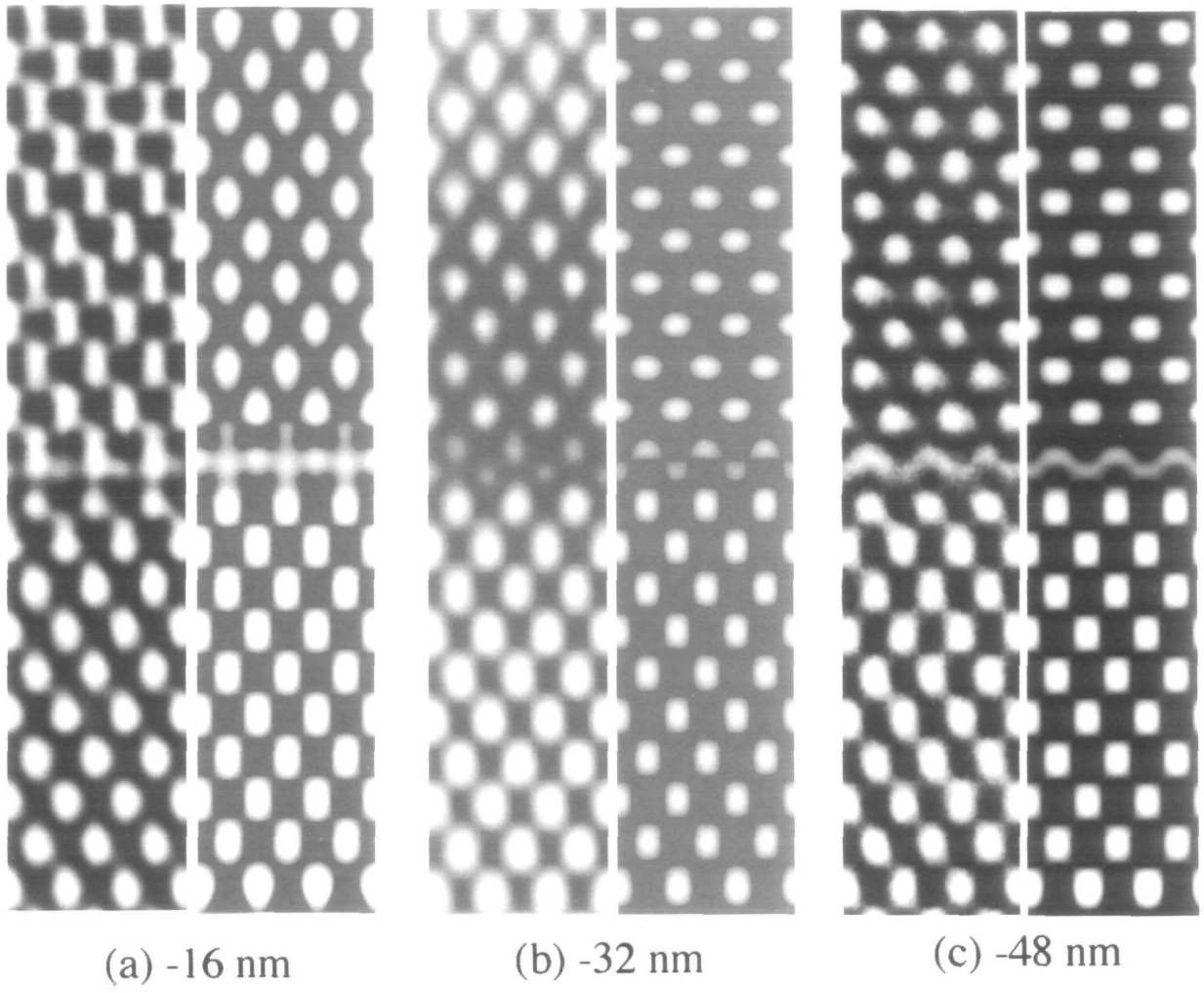

Fig. 8 Experimental images (left-hand side) and simulated images of V(r) (right-hand side) for defocus values (a) –16, (b) –32 and (c) –48 nm, respectively.

$$\ln(V(r)/D(r)) = -1 - \lambda_0 - \sum_j \lambda_j (2\sigma)^* f(T(H)) \quad (9)$$

and $$\lambda_j e_j - 2\mu_j(e_j/\sigma_j^2 = 0 \quad (10)$$

so that $$e_j = \lambda_j(\sigma_j/2\mu_j) \quad (10')$$

From Eq. (9)

$$V(r) = D(r)\exp(-1 - \lambda_0)\exp(-2\sigma \sum_j \lambda_j^* f(T(H))) \quad (11)$$

Using the first constraint in Eq. (6)

$$\sum_i V(r) = f = \sum_i D(r)\exp(-1 - \quad (12)$$

$$\lambda_0)\exp(-2\sigma \sum_j \lambda_j^* f(T(H)))$$

Therefore

$$\exp(-1 - \lambda_0) = \frac{f}{\sum_i D(r)\exp(-2\sigma \sum_j \lambda_j^* f(T(H)))}$$

The optimum solution of V(r) becomes

$$V(r) = \frac{fD(r)\exp(-2\sigma \sum_j \lambda_j^* f(T(H)))}{\sum_i D(r)\exp(-2\sigma \sum_j \lambda_j^* f(T(H)))}$$

The problem is finding sets of good values of λ_j and μ_j for different defocus images, which are then substituted into the above equation to get the optimum V(r).

From Eq. (7), the optimum λ_j must satisfy the following

$$1 + 2\sigma V(r)^* f(T(H)) - I_j^e - e_j = 10 \quad (13)$$

Substituting (10′) into (13), let

$$I_j^{pred} = 1 + 2\sigma V(r)*f(T(H))$$

$$I_j^{pred} - I_j^e = \lambda_j \frac{\sigma_j^2}{2\mu_j} \qquad (14)$$

$$\frac{1}{4\mu_j^2} \sum_j \sigma_j^2 \lambda_j^2 - \Omega = 0 \qquad (15)$$

The Eq. (14) and Eq.(15) are the gradients of a potential function of Z with respect to λ_j and μ_j. The function Z is defined as the following:

$$Z = \sum_j \lambda_j - \log\{ \sum_i \exp(-2\sigma \sum_j \lambda_j * f(T(H)))\} -$$

$$\frac{1}{4\mu_j^2} \sum_j \sigma_j^2 \lambda_j^2 - \lambda_j I_j^e - \mu_j \Omega$$

The λ_j's and μ_j's can then be determined from $\partial Z/\partial\lambda_j = 0$ and $\partial Z/\partial\mu_j = 0$, and substituted to give the optimum solution of V(r).

After finding V(r), the I_j^{pred} can be determined. In the iterations of constrained-MEM, we get an initial estimate of V(r) from a Wiener filter and use this to calculate I_j^{pred}. The $\delta\lambda_j$ and $\delta\mu_j$ can be determined from the difference between I_j^{pred} and I^e_j and minimization of Z. The Z function was minimized using the conjugated gradient technique [35]. The new V $(x, y)$is then re-evaluated and goes to the other iteration. After each iteration a figure of merit χ^2 function is calculated.

$$\chi^2 = \frac{(I_j^{pred} - C I_j^e)^2}{\sigma_j^2}$$

C is a normalization factor equal to the ratio of the means of two successive images. If convergence occurs, the χ^2 becomes smaller in each iteration. A flow chart of the MEM iteration is given in Fig. 3. The above constrained-MEM algorithm was programmed in 'Digital Micrograph' in a Macintosh computer.

As mentioned in the earlier section and shown in Fig. 1c, the constrained-MEM not only improves the phases of V(r) within the present frequencies, but also extrapolates the phases to the next higher order beams. The optimum V(r) is then Fourier transformed to reciprocal space, and square root intensities from the high order diffraction spots in the diffraction pattern are substituted into the corresponding diffraction beams. The real space (constrained-MEM) and reciprocal space constraints are operated cyclically until the satisfaction level is reached.

Results and discussion

The Si HRTEM images in Fig. 2a were used as a test example for our method. The dumb-bell structure of Si is not revealed in the HRTEM image shown in Fig. 2a, since the projected distance of the dumb-bell structure is 0.135 nm along a <110> zone axis. Using the diffraction pattern in Fig. 2c and the Wiener filtered image shown in Fig. 2d as a starting V(r), the dumb-bell structure can be revealed through the algorithm described above. The order of diffraction of the Si in a <110> zone axis is {111}, {002}, {220}, {113}, {222}, {004} . . . which corresponds to the frequency of 3.18, 3.69, 5.21, 6.09, 6.37, 7.35 nm^{-1}, respectively. The measured square root intensities up to {004} are given in the first column of Table 1. The measured intensity of each diffraction is obtained by summing a total of 10×10 pixels box around each diffraction spot. The square root intensities are normalized with respect to {111} in Table 1. The calculated structure factors and the calculated amplitudes of the diffracted beams for a thickness of 8 nm are given in the second and third column of Table 1, respectively. The amplitudes of the diffracted beams were calculated using a multislice program [36]. The {002} and {222} reflections are kinematically forbidden. Even though very weak intensities of {002} and {222} were recorded in the diffracted pattern, the ratios of measured amplitudes are reasonably close to those of but kinematical structural factors and thin specimens. This may suggest that the linear imaging constraint in the MEM may be applicable for this case, and the Babinet function, $|1-\psi(r)|$, may be closely related to the projected potential V(r).

The V(r) is extended to spatial frequencies of 3.2, 5.2, 6.1, 6.4 and 7.5 nm^{-1} using the constrained-MEM. The results are shown in Fig. 4. In Fig. 4, the Fourier transforms of each V(r) of different resolutions are also included. The dumb-bell structure is clearly revealed at a frequency of 7.35 nm^{-1}.

The constrained-MEM was applied to solve the atomic structure of an epitaxial $NiSi_2$/Si interface. Epitaxial $NiSi_2$ thin films were grown by depositing 30 nm of metal nickel on phosphorus-doped (001) oriented Si wafers, followed by isothermal annealing in a three zone furnace at 800°C in ambient N_2 for 20 min. High-resolution imaging was carried out in a JEOL 4000EX microscope. Figure 5 shows HRTEM images of an $NiSi_2$/Si interface recorded under three different under-focus values, Δf, −16 nm, −32 nm and −48 nm, taken near the edge of the specimen along the [110] zone axis. The focus values were estimated from the minimum contrast of the amorphous material at the edge of the specimen. $NiSi_2$ has a face-centred cubic unit cell with the CaF_2 structure and lattice constant a = 0.5406 nm. Si has the diamond cubic structure with lattice constant a = 0.543 nm. They have 0.4% of lattice misfit. Eight possible geometrical models of $NiSi_2$/Si can be deduced from the coincidence-site lattice model and are given in Fig. 6 [2]. None of the three images of Fig. 5 show a dumb-bell structure, so the structure of the interface cannot directly be read out from the images. The interfacial structure was determined

from trial-and-error by simulating the images for every possible model. Model (h) was found to fit all three experimental images. The insets pasted in Fig. 5 are simulated images calculated by the multislice method using MacTempas [36] for each under-focus value.

The MEM deduced V(r) of the $NiSi_2$/Si interface at a spatial frequency of 7.35 nm^{-1} is shown in Fig. 7. The dumb-bell structures of both $NiSi_2$ and Si are clearly seen. The atomic structure of the interface can be directly read out and is the same as model (h) in Fig. 6. Model (h) is superimposed with the V(r) in Fig. 7. The simulated images of V(r) for each different defocus are given in Fig. 8 to compare with the experimental images. It can be seen that the MEM-deduced V(r) gives reasonably close agreement between the simulated images and the experimental images.

In order to solve the atomic structure of an interface using the algorithm here, no a priori knowledge of the interface is needed, provided that a good diffraction pattern and a (or a series of) HRTEM image(s) are well recorded. However, there are some factors which may cause difficulties in the application of this method. Local bending of the specimen may destroy the symmetry in intensities in the diffraction pattern. Furthermore, even with special care in aligning the crystal axis, the same set of diffraction spots, for example, {111}, still has about 10–15% difference in intensity. This arises because the sensitivity of the eye is not as good as the imaging plate. The measured intensities from the same set of diffraction spots were averaged in the present work since we know the bulk structures are centro-symmetrical. However, this may cause difficulties in non-centro-symmetric materials.

Even though the atomic structure of the $NiSi_2$/Si interface can be revealed using the constrained-MEM algorithm, the intensities in the Ni and Si atomic peaks in Fig. 7 do not have any particular relationship, such as proportionality to the ratio of atomic number. As mentioned earlier, this method only reveals the possible atomic peaks, but not the exact form of the exit wave. This may be because quasi-kinematical data were used for the linear imaging constraint in the MEM. Dynamical diffraction becomes more important in higher order diffraction [19], which may cause the linear imaging constraint in our MEM algorithm at high spatial frequencies to break down. For future development of the method, the linear imaging constraint in the MEM algorithm will be extended to a general complex wave case and improved to a non-linear imaging constraint.

Conclusions

A linear imaging constrained-MEM has been developed to extend the resolution from a series of defocused high-resolution images and one diffraction pattern. The algorithm of this method is basically the Gerchberg–Saxton algorithm, which restores spatial information by imposing Fourier space and real space constraints cyclically. The method has been applied to retrieve the atomic peaks of a $NiSi_2$/Si interface from a series of under-focus images. No a priori information of structural models is needed for this process.

Acknowledgements

The authors would like to thank the National Science Council for financial support. F.R.C. would like to thank Professor L.D. Marks for helpful discussion and encouragement.

References

1 Chang H, Chang L, Chen F -R, Kai J J, Tzou E, Fu J, Xu Z, Egermeier J, and Chen F -S (1998) High resolution and energy filtering TEM study of interfacial structure and reaction in advanced materials processing. *Acta Mater.* **46:** 2431–2439.

2 Chen W J and Chen F -R (1993) The atomic structure of $\Sigma=1$ and $\Sigma=3$ $NiSi_2$/Si interface. *Philos Mag.* **68A:** 605–630.

3 Chen F -R, Chu C C, Wang J Y, and Chang L (1995) Atomic structure of $\Sigma7$ (0112) symmetrical tilt grain boundaries in α-Al_2O_3. *Philos. Mag.* **782:** 529–544.

4 Hoche T, Kenway P R, Kleebe H -J, and Ruhle M (1994) High-resolution transmission electron microscopy studies of a near $\Sigma11$ grain boundary in α-alumina. *J Am Ceram. Soc.* **77:** 339–348.

5 Hofmann D and Ernst F (1994) Quantitative high-resolution transmission electron microscopy of the incoherent $\Sigma3$ (211) boundary in Cu. *Ultramicroscopy* **53:** 205–221.

6 Buseck P, Cowley J, and Eyring L (1988) *High Resolution Transmission Electron Microscopy and Associated Techniques* (Oxford University Press, Oxford).

7 Spence J C H (1988) *Experimental High-Resolution Electron Microscopy.* (Oxford University Press, Oxford).

8 Coene W, Janssen A J E M, Op de Beeck M, and Van Dyck D (1995) Improving HRTEM performance by digital processing of focal image series: results from the CM20 FEG-super TWIN. *Philips Electron Optics Bull.* **132:** 15–28.

9 Van Dyck D, Lichte H, and Van der Mast K D (1996) Sub-angstrom structure characterisation: the Brite-Euram route towards one angstrom. *Ultramicroscopy* **64:** 1–15.

10 Kirkland E J (1982) Nonlinear high resolution image processing of conventional transmission electron micrographs. *Ultramicroscopy* **9:** 45–64.

11 Thust A, Lentzen M, and Urban K (1994) Non-linear reconstruction of the exit plane wave function from periodic high resolution electron microscopy images. *Ultramicroscopy* **53:** 101–120.

12 Thust A, Coene W M J, Op de Beeck M, and Van Dyck D (1994) Focal-series reconstruction in HRTEM: simulation studies on non-periodic objects. *Ultramicroscopy* **64:** 211–230.

13 Ishizuka K, Miyazaka M, and Uyeda N (1982) Improvement of electron microscope images by the direct phasing method. *Acta Cryst.* **A38:** 408–413.

14 Fan H -F, Zhong Z Y, Zheng C -D, and Li F -H (1985) Image processing in high resolution electron microscopy using the direct method. I. Phase extension. *Acta Cryst.* **A51:** 163–165.

15 Fan H -F, Xiang S B, Li F H, Pan Q, Uyeda N and Fujiyoshi Y (1991) Image-resolution enhancement by combining information from electron-diffraction pattern and micrograph. *Ultramicroscopy* **36:** 361–365.

16 Hu J J, Li F H, and Fan H F (1992) Crystal structure determination of K_2O-bullet Nb_2O_5 by combining high resolution electron microscopy and electron diffraction. *Ultramicroscopy* **41:** 287–397.

17 Huang D X, He W Z, and Li F H (1996) Multiple solution in maximum entropy deconvolution of high-resolution electron microscope images. *Ultramicroscopy* **62:** 141.

18 Dong W, Baird T, Fryer J R, Gilmore C J, MacNicol D D, Bricogne G, Smith D J, O'Keefe M A, and Hovmoller S (1992) Electron microscopy

at 1 A resolution by entropy maximization and likelihood ranking. *Nature* **355:** 605–609.

19 Sinkler W, Bengu E, and Marks L D (1998) Application of direct methods to dynamical electron diffraction data for solving bulk crystal structures. *Acta Cryst.* **A54:** 591–605.

20 Sayre D (1980) Phase extension and refinement using convolutional and related equation system: In: *Theory and Practice of Direct Methods in Crystallography.* eds Ladd M F C and Palmer R A, pp. 271–286, (Plenum Press, New York).

21 Hoppe W and Gassmann J (1968) Phase correction, a new method to solve partially known structures. *Acta Cryst.* **B24:** 97–108.

22 Gassmann J and Zechmeister K (1972) Limits of phase expansion in direct methods. *Acta Cryst* **A28:** 270–280.

23 Dorset D, Jap B K, Ho M H, and Glaeser R M (1979) Direct phasing of electron diffraction data from organic crystals: effect of n-beam dynamical scattering. *Acta Cryst A* **35:** 1001–1009.

24 Debaerdemeker K, Tate C, and Woolfson M M (1985) On the application of phase relationship to complex structures. XXIV. The Sayre Tangent formula. *Acta Cryst.* **A41:** 286–290.

25 Bricogne G (1984) Maximum entropy and the foundations of direct methods. *Acta Cryst* **A40:** 410–445.

26 Marks L D and Landree E A (1998) Minimum-entropy algorithm for surface phasing problem. *Acta Cryst.* **A54:** 296–305.

27 Marks L D, Bengu E, Collazo-Davlia C, Grozea D, Landree E, Leslie C, and Sinkler W (1998) Direct methods for surfaces. *Surface Rev Lett.* **5:** 1087–1106.

28 Levi A and Strak H (1987) Restoration from phase and magnitude by generalized projections. In: *Image Recovery: Theory and Application,* ed. Stark H, pp. 227–320, (Academic Press, London).

29 Gatan Inc., 6678 Owens Dr, Pleasanton, CA 94588-3334, USA Digital Micrograph is an image processing program produced by Gatan Inc. (1991)

30 Gonzalez R C and Woods R E (1993) *Digital Image Processing,* pp. 253–304, (Addison-Wesley, Reading, MA, USA).

31 Wilczek R and Drapatz S (1985) A high accuracy algorithm for maximum entropy image restoration in the case of small data sets. *Astron. Astrophys.* **142:** 9–12.

32 Cornwell T J and Evans K F (1985) A simple maximum entropy deconvolution algorithm. *Astron Astrophys.* **143:** 77–85.

33 Imaging plate system is a product of Fuji Company, Japan.

34 Kai J J and Chen F -R (1998) High performance electron microscopy applications in advanced energy materials. In: *Proceedings of International Symposium on Advanced Energy Technology, February 2–4, 1998, Sapporo, Japan.*

35 Press H W, Teukolsky S A, Vetterling W T, and Flannery B P (1992) *Numerical Recipes,* pp. 431–418, (Cambridge University Press).

36 Kilaas R (1991) The MacTemp HRTEM image simulation program is written by R Kilaas, Total Resolution Co., CA, USA.